



# A molecular quantum switch based on tunneling in *meta*-D-phenol C<sub>6</sub>H<sub>4</sub>DOH†

Cite this: *Phys. Chem. Chem. Phys.*, 2018, 20, 7387

Received 8th January 2018,  
Accepted 7th February 2018

DOI: 10.1039/c8cp00133b

rsc.li/pccp

Csaba Fábri,<sup>a</sup> Sieghard Albert,<sup>c</sup> Ziqiu Chen,<sup>b</sup> Robert Prentner<sup>c</sup> and Martin Quack<sup>b,\*c</sup>

**We introduce the concept of a molecular quantum switch and demonstrate it with the example of *meta*-D-phenol, based on recent theoretical and high-resolution spectroscopic results for this molecule. We show that in the regime of tunneling switching with localized low-energy states and delocalized high-energy states the molecular quantum switch can be operated in two different ways: (i) a quasiclassical switching by coherent infrared radiation between the two isomeric structures *syn*- and *anti*-*m*-D-phenol; and (ii) a highly nonclassical switching making use of bistructural quantum superposition states of the *syn* and *anti* structures, which can be observed by their time-dependent spectra after preparation.**

## 1 Introduction

Molecular switches and machines have received much attention and undergone a substantial development over the last few decades (see ref. 1 and references cited therein). Typical examples are provided by *cis*-*trans* isomerizations as in azobenzene derivatives<sup>2–10</sup> or in the retinal framework as used in bacteriorhodopsin or in vision,<sup>11</sup> perhaps even prototypical for thought processes, the eye being considered by some to be part of the brain.<sup>12</sup> Chiral modifications of these or intrinsically chiral molecules can be used in chiroptical switches.<sup>13</sup> Molecular switches can be utilized to open and close molecular containers.<sup>14</sup> These switches are frequently driven by photoisomerisation employing visible or UV light, but more general chemical concepts have been applied and extensions to molecular motors and machines exist.<sup>15–21</sup> Common to all of these developments is the change of essentially “classical” molecular structures initiated by some external driving mechanism.

A different type of “switch” would be the change in the population of molecular quantum states driven by coherent radiation, as occurs in a wide variety of situations ranging from the spin states in magnetic resonance (see ref. 22, 23 and references cited therein) to optically driven population transfers (see ref. 24–29 and references cited therein). In these cases structural properties are irrelevant and the induced changes could refer to the spin states, rotation–vibration or electronic states of molecules or even single atoms or ions.

A simple one-dimensional model combining these two basic concepts was proposed some time ago in terms of coherent quantum wavepacket motion showing the transient chirality of a hypothetical chiral molecular quantum switch, however, without a realistic molecular background,<sup>30</sup> and the principle of chiral molecular quantum switches has been discussed also in relation to parity violation in chiral molecules, with possible application towards experiments in fundamental molecular quantum physics,<sup>25,31,32</sup> but no immediately obvious application towards a possible molecular quantum technology.

In the present work we introduce a realistic prototypical example of a molecular quantum switch based on a structural change in *meta*-D-phenol, which was recently shown to exhibit the phenomenon of tunneling switching with excitation in the infrared spectral range.<sup>33,34</sup> As illustrated in Fig. 1, this molecule shows localized quantum states at low vibrational energies but can be switched between localized states when excited to higher energies where tunneling switching occurs, corresponding to delocalized, truly bistructural states. As we shall show, using coherent excitation with electromagnetic radiation one can generate a genuine molecular quantum switch, which includes the possibilities of localized quasiclassical structures of low energy eigenstates, delocalized structures of excited torsional states and bistructural quantum superposition states. The properties of such molecular quantum switches thus include both the properties of quasiclassical molecular structures and quantum superposition states as they might find applications in quantum information and computing.<sup>35</sup>

<sup>a</sup> Laboratory of Molecular Structure and Dynamics, Institute of Chemistry, Eötvös University, Pázmány Péter sétány 1/A, H-1117 Budapest, Hungary

<sup>b</sup> MTA-ELTE Complex Chemical Systems Research Group, P.O. Box 32, H-1518 Budapest 112, Hungary

<sup>c</sup> Physical Chemistry, ETH Zürich, CH-8093 Zürich, Switzerland.

E-mail: martin@quack.ch; Fax: +41-44-632-1021; Tel: +41-44-632-4421

† Electronic supplementary information (ESI) available: Potential energy data. See DOI: 10.1039/c8cp00133b

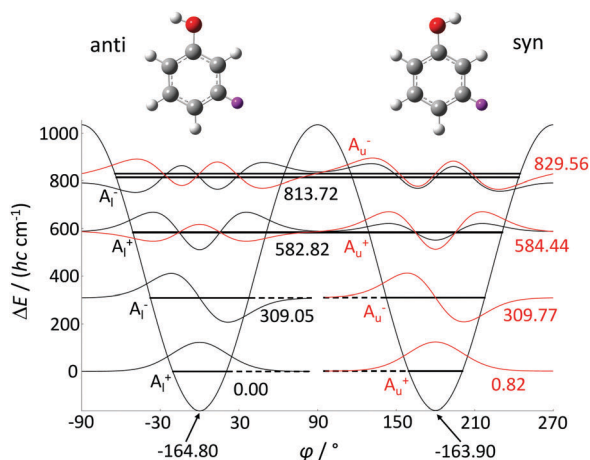


**Fig. 1** The lowest adjusted adiabatic channel potential for *meta*-D-phenol including several torsional energy levels and wavefunctions. The two potential wells corresponding to the *anti* and *syn* structures are indicated by the two equilibrium structures (carbon atoms are shown in grey, hydrogen light grey, oxygen red and deuterium violet). The subscripts l and u refer to lower and upper levels, whose energies are referenced to the lowest quantum state as 0 and are given in terms of  $E_k/(hc \text{ cm}^{-1})$ . The superscripts + and – denote positive and negative parities. In the graphical representation the splittings can be seen only for the highest level but can be deduced from the energies given. The two minima of the adiabatic channel potentials are indicated by their negative values with respect to the energy zero.

## 2 Theory and computational aspects

We treat the quantum dynamics of *m*-D-phenol with a purely vibrational model, as this contains the essence of the effects to be demonstrated. In the real system, rotation can be easily added using the usual rotation–vibration Hamiltonian and selection rules,<sup>36</sup> which have been shown to provide an excellent representation of the high-resolution spectra of *m*-D-phenol<sup>34</sup> and also of phenol<sup>33</sup> in this spectral range. We follow ref. 25 in the theoretical treatment, where the explicit inclusion of rotation has also been discussed (for CIOCl). The full-dimensional quantum dynamics are treated in two steps. First, we solve the time-independent vibrational Schrödinger equation (1) using the quasiadiabatic channel reaction path Hamiltonian approximation (RPH) treating the torsional coordinate as the large-amplitude reaction path.<sup>25,33,34,37–39</sup> The theoretical data of ref. 34 and 251 equidistant discrete variable representation (DVR)<sup>40</sup> points along the torsional angle  $\varphi$  (see Fig. 1 for the definition of  $\varphi$ ) have been used to solve the vibrational Schrödinger equation

$$\hat{H}_0(\mathbf{x})\phi_k(\mathbf{x}) = E_k\phi_k(\mathbf{x}) \quad (1)$$

providing vibrational energy levels  $E_k$  and wavefunctions  $\phi_k(\mathbf{x})$ , where  $\mathbf{x}$  represents the complete set of internal coordinates (including torsion). The ground-state channel potential was adjusted to better represent the experimental energy level differences for *m*-D-phenol<sup>34</sup> by shifting the two parts of the potential derived *ab initio*<sup>33,34</sup> by the same amount but in opposite directions. The optimal shift parameter was determined to be  $0.34 \text{ cm}^{-1}$  for  $-90^\circ < \varphi < 90^\circ$  and  $-0.34 \text{ cm}^{-1}$  for

$90^\circ < \varphi < 270^\circ$ . The corresponding effective channel potentials are given in the ESI† in Table A1.

In the second step we solve the time-dependent Schrödinger equation ( $i = \sqrt{-1}$ )

$$i\frac{\hbar}{2\pi}\frac{\partial\Psi(\mathbf{x},t)}{\partial t} = \hat{H}(\mathbf{x},t)\Psi(\mathbf{x},t) \quad (2)$$

with

$$\hat{H}(\mathbf{x},t) = \hat{H}_0(\mathbf{x}) + \hat{V}(\mathbf{x},t), \quad (3)$$

where  $\hat{H}_0(\mathbf{x})$  is the Hamiltonian of the isolated molecule and the interaction of the molecule with a time-dependent coherent quasiclassical quasiperiodic electric field  $\vec{E}(t)$  is described by

$$\hat{V}(\mathbf{x},t) = -\vec{\mu}(\mathbf{x})\vec{E}(t), \quad (4)$$

corresponding to the electric dipole approximation. The time-dependent wavefunction

$$\Psi(\mathbf{x},t) = \sum_k a_k(t)\phi_k(\mathbf{x}) \quad (5)$$

is expanded in the eigenstate basis  $\phi_k(\mathbf{x})$ . In practice, a coupled set of first-order linear differential equations for the coefficients  $a_k(t)$  in the eigenstate basis (using the interaction picture) has to be solved<sup>24</sup>

$$i\frac{\hbar}{2\pi}\dot{a}_j(t) = \sum_k V_{jk}(t)\exp(i\omega_{jk}t)a_k(t) \quad (6)$$

with  $\omega_{jk} = 2\pi(E_j - E_k)/\hbar$ . For the time-dependent quantum-dynamical calculations we have employed a Gaussian intensity distribution of the laser pulse

$$I(t) = I_{\max}\exp(-2(t - t_0)^2/\tau_P^2), \quad (7)$$

where  $I_{\max}$  is the maximum intensity reached at time  $t_0$  and  $\tau_P$  determines the length of the laser pulse. Assuming linearly polarized light the Gaussian envelope gives rise to a time-dependent electric field

$$\vec{E}(t) = \vec{e}\sqrt{\frac{2I_{\max}}{c\epsilon_0}}\cos(\omega_0 t)\exp(-(t - t_0)^2/\tau_P^2), \quad (8)$$

where  $\vec{e}$ ,  $\omega_0$  and  $c$  denote the polarization vector, the angular carrier frequency of the laser and the speed of light in vacuum, respectively. The coupled first-order differential equations of eqn (6) were integrated numerically with the Mathematica program package.<sup>41</sup> For the general background and details of the methods and practical approximations we refer to ref. 24, 25 and 42.

In the results we show time-dependent probability densities  $|\Psi(\varphi,t)|^2$ , the time-dependent populations  $p_k = |a_k|^2$  and the time-dependent absorption spectra in terms of the reduced normalized absorption cross section

$$\sigma_{\text{rel}}(\tilde{\nu}) = |\mu_{if}|^2 \exp(-4 \ln 2 (\tilde{\nu} - \tilde{\nu}_0)^2/\tilde{\gamma}^2) \sqrt{\pi(\tilde{\gamma}/\text{cm}^{-1})^2/(4 \ln 2)},$$

where  $|\mu_{if}|^2$  is the value of the relative (reduced) dimensionless absolute square of the electric dipole transition moment between the initial and final eigenstates, and the spectral line

is centered at  $\tilde{\nu}_0$  with a full width at half maximum  $\tilde{\gamma}$  (both given as wavenumbers in  $\text{cm}^{-1}$ ).

## 3 Results

### 3.1 Time-independent results

The experimental and theoretical energy levels corresponding to the *ab initio* and adjusted ground-state channel potentials are given in Table 1, whereas vibrational electric dipole matrix elements are presented in Table 2. The electric dipole matrix elements of Table 2 have been computed using the adjusted ground-state channel potential and are referenced in the principal axis frame (with  $x = c$ ,  $y = b$  and  $z = a$ , where  $z$  is oriented along the CO bond and the  $yz$  plane forms the benzene ring plane<sup>34</sup>).

### 3.2 Wavepacket dynamics (with the vibrational ground state as the initial state)

For the coherent excitation we use linear polarization along the  $z(a)$  axis throughout Section 3.2 (unless otherwise stated) with the ground state as the initial state. The “wavepackets” are represented as probability proportional to probability density ( $|\Psi(\varphi, t)|^2 d\varphi$  with a nominal value of  $d\varphi = 1^\circ$ ).

#### 3.2.1 Two-pulse excitation scheme: $|0_{anti}\rangle \rightarrow |2_{lower}\rangle \rightarrow |0_{syn}\rangle$ .

This excitation scheme corresponds to a stimulated resonance Raman-like process and switches between the two molecular structures corresponding to the two lowest localized eigenstates of the quantum switch. The frequencies are chosen to be in exact resonance for the absorption and stimulated emission pulses. Fig. 2 shows the time evolution of the wavepacket (reduced probability density as a function of the torsional angle  $\varphi$  and time  $t$ ) and selected eigenstate populations. The result of this excitation scheme is a quasiclassical switching between the *anti* and the *syn* isomers (and the corresponding localized ground states  $|0_{anti}\rangle$  and  $|0_{syn}\rangle$ ) with the help of an intermediate delocalized state  $|2_{lower}\rangle$  which is radiatively coupled to both  $|0_{anti}\rangle$  and  $|0_{syn}\rangle$ . The *anti* and *syn* “states” of the switch can be distinguished by measuring the infrared spectrum of the

**Table 2** Vibrational electric dipole moment matrix elements referenced in the principal axis frame (see text). Missing values are zero due to symmetry

State <sub>1</sub>	State <sub>2</sub>	$\mu_x/D$	$\mu_y/D$	$\mu_z/D$
$ 0_{anti}\rangle$	$ 0_{syn}\rangle$		$1.947 \times 10^{-3}$	$7.103 \times 10^{-5}$
$ 0_{anti}\rangle$	$ 1_{anti}\rangle$	$3.497 \times 10^{-1}$		
$ 0_{anti}\rangle$	$ 1_{syn}\rangle$	$1.665 \times 10^{-2}$		
$ 0_{anti}\rangle$	$ 2_{lower}\rangle$		$4.845 \times 10^{-2}$	$3.480 \times 10^{-2}$
$ 0_{anti}\rangle$	$ 2_{upper}\rangle$		$-3.185 \times 10^{-2}$	$-2.287 \times 10^{-2}$
$ 0_{anti}\rangle$	$ 3_{lower}\rangle$	$1.240 \times 10^{-2}$		
$ 0_{anti}\rangle$	$ 3_{upper}\rangle$	$-1.189 \times 10^{-2}$		
$ 0_{anti}\rangle$	$ 4_{lower}\rangle$		$3.674 \times 10^{-3}$	$4.559 \times 10^{-3}$
$ 0_{anti}\rangle$	$ 4_{upper}\rangle$		$-3.208 \times 10^{-3}$	$-4.302 \times 10^{-3}$
$ 0_{syn}\rangle$	$ 1_{anti}\rangle$	$1.666 \times 10^{-2}$		
$ 0_{syn}\rangle$	$ 1_{syn}\rangle$	$-3.498 \times 10^{-1}$		
$ 0_{syn}\rangle$	$ 2_{lower}\rangle$		$-3.341 \times 10^{-2}$	$2.043 \times 10^{-2}$
$ 0_{syn}\rangle$	$ 2_{upper}\rangle$		$-5.079 \times 10^{-2}$	$3.126 \times 10^{-2}$
$ 0_{syn}\rangle$	$ 3_{lower}\rangle$	$-1.199 \times 10^{-2}$		
$ 0_{syn}\rangle$	$ 3_{upper}\rangle$	$1.230 \times 10^{-2}$		
$ 0_{syn}\rangle$	$ 4_{lower}\rangle$		$-3.987 \times 10^{-3}$	$4.256 \times 10^{-3}$
$ 0_{syn}\rangle$	$ 4_{upper}\rangle$		$-3.521 \times 10^{-3}$	$4.078 \times 10^{-3}$
$ 1_{anti}\rangle$	$ 1_{syn}\rangle$		$-1.106 \times 10^{-1}$	$-4.020 \times 10^{-3}$
$ 1_{anti}\rangle$	$ 2_{lower}\rangle$	$4.365 \times 10^{-1}$		
$ 1_{anti}\rangle$	$ 2_{upper}\rangle$	$-2.572 \times 10^{-1}$		
$ 1_{anti}\rangle$	$ 3_{lower}\rangle$		$7.478 \times 10^{-2}$	$5.202 \times 10^{-2}$
$ 1_{anti}\rangle$	$ 3_{upper}\rangle$		$7.921 \times 10^{-2}$	$4.718 \times 10^{-2}$
$ 1_{anti}\rangle$	$ 4_{lower}\rangle$	$3.185 \times 10^{-2}$		
$ 1_{anti}\rangle$	$ 4_{upper}\rangle$	$-2.503 \times 10^{-2}$		
$ 1_{syn}\rangle$	$ 2_{lower}\rangle$	$-2.573 \times 10^{-1}$		
$ 1_{syn}\rangle$	$ 2_{upper}\rangle$	$-4.365 \times 10^{-1}$		
$ 1_{syn}\rangle$	$ 3_{lower}\rangle$		$8.319 \times 10^{-2}$	$-4.030 \times 10^{-2}$
$ 1_{syn}\rangle$	$ 3_{upper}\rangle$		$-7.754 \times 10^{-2}$	$4.760 \times 10^{-2}$
$ 1_{syn}\rangle$	$ 4_{lower}\rangle$	$-2.885 \times 10^{-2}$		
$ 1_{syn}\rangle$	$ 4_{upper}\rangle$	$-2.771 \times 10^{-2}$		
$ 2_{lower}\rangle$	$ 2_{upper}\rangle$		$9.458 \times 10^{-1}$	$3.424 \times 10^{-2}$
$ 2_{lower}\rangle$	$ 3_{lower}\rangle$	$6.208 \times 10^{-1}$		
$ 2_{lower}\rangle$	$ 3_{upper}\rangle$	$1.175 \times 10^{-1}$		
$ 2_{lower}\rangle$	$ 4_{lower}\rangle$		$-3.485 \times 10^{-2}$	$-8.587 \times 10^{-2}$
$ 2_{lower}\rangle$	$ 4_{upper}\rangle$		$1.560 \times 10^{-1}$	$2.388 \times 10^{-2}$
$ 2_{upper}\rangle$	$ 3_{lower}\rangle$	$1.185 \times 10^{-1}$		
$ 2_{upper}\rangle$	$ 3_{upper}\rangle$	$-6.170 \times 10^{-1}$		
$ 2_{upper}\rangle$	$ 4_{lower}\rangle$		$1.818 \times 10^{-1}$	$-1.086 \times 10^{-2}$
$ 2_{upper}\rangle$	$ 4_{upper}\rangle$		$3.598 \times 10^{-2}$	$-8.766 \times 10^{-2}$
$ 3_{lower}\rangle$	$ 3_{upper}\rangle$		$8.716 \times 10^{-1}$	$3.141 \times 10^{-2}$
$ 3_{lower}\rangle$	$ 4_{lower}\rangle$	$7.756 \times 10^{-1}$		
$ 3_{lower}\rangle$	$ 4_{upper}\rangle$	$-1.000 \times 10^{-2}$		
$ 3_{upper}\rangle$	$ 4_{lower}\rangle$	$1.130 \times 10^{-2}$		
$ 3_{upper}\rangle$	$ 4_{upper}\rangle$	$7.202 \times 10^{-1}$		
$ 4_{lower}\rangle$	$ 4_{upper}\rangle$		$6.728 \times 10^{-1}$	$2.409 \times 10^{-2}$

**Table 1** Experimental and theoretical reaction path Hamiltonian energy levels corresponding to the pure *ab initio* and adjusted ground-state channel potentials. The labeling of energy levels reflects tunneling switching, with  $|2_{lower}\rangle$  and  $|2_{upper}\rangle$  being the first two delocalized vibrational states (see Fig. 1). Differences between neighboring energy levels are given in parentheses. The *ab initio* and adjusted zero point energies with respect to the individual minima are  $164.72(hc \text{ cm}^{-1})$  (*syn*) and  $164.80(hc \text{ cm}^{-1})$  (*anti*)

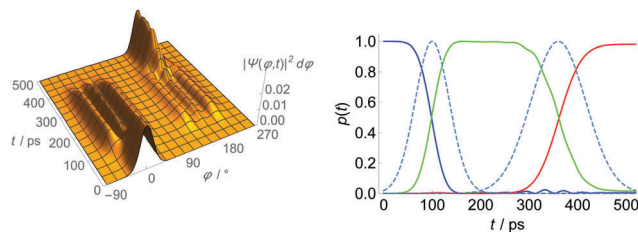
State	$E_{\text{experimental}}/(hc \text{ cm}^{-1})$	$E_{\text{ab initio}}/(hc \text{ cm}^{-1})$	$E_{\text{adjusted}}/(hc \text{ cm}^{-1})$
$ 0_{anti}\rangle$	0.00	0.00	0.00
$ 0_{syn}\rangle$	0.82 (0.82)	1.50 (1.50)	0.82 (0.82)
$ 1_{anti}\rangle$	309.24	309.05	309.05
$ 1_{syn}\rangle$	309.97 (0.73)	310.45 (1.40)	309.77 (0.72)
$ 2_{lower}\rangle$	585.19	582.97	582.82
$ 2_{upper}\rangle$	586.91 (1.72)	584.96 (1.99)	584.44 (1.62)
$ 3_{lower}\rangle$		814.04	813.72
$ 3_{upper}\rangle$		829.92 (15.88)	829.56 (15.84)
$ 4_{lower}\rangle$		980.17	979.83
$ 4_{upper}\rangle$		1056.44 (76.26)	1056.10 (76.26)

molecule. Simulated spectra for the two isomers in two different spectral ranges are shown in Fig. 3.

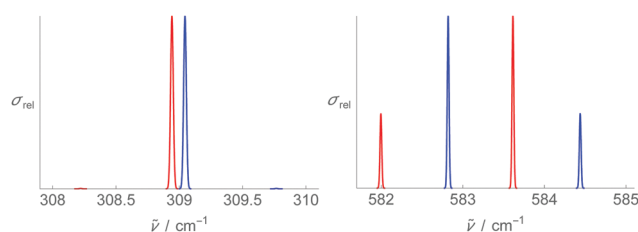
#### 3.2.2 Excitation scheme: $|0_{anti}\rangle \rightarrow |2_{lower}\rangle$ and $|2_{upper}\rangle$ .

Fig. 4 shows the initial time evolution of the wavepacket and selected eigenstate populations, while Fig. 5 depicts the subsequent field-free time evolution of the coherent superposition of  $|2_{lower}\rangle$  and  $|2_{upper}\rangle$  generated by the laser pulse. The motion of the wavepacket shown in Fig. 5 thus corresponds to tunneling isomerization at about  $583 \text{ cm}^{-1}$ . The isomerization time is about 10 ps ( $t_T = h/(2\Delta E_{\text{el}})$ ) as expected. The populations of  $|2_{lower}\rangle$  and  $|2_{upper}\rangle$  are not equal because of the asymmetry in the eigenstates and electric dipole matrix elements.

**3.2.3 Two-pulse excitation scheme:  $|0_{anti}\rangle \rightarrow |2_{lower}\rangle \rightarrow |0_{anti}\rangle$  and  $|0_{syn}\rangle$ .** This excitation scheme corresponds to the preparation of a bistructural coherent superposition state of the  $|0_{anti}\rangle$  and  $|0_{syn}\rangle$  states at the end of the process. Fig. 6 shows the time



**Fig. 2** Time-dependent wavepacket (reduced probability density as a function of the torsional angle  $\varphi$  and time  $t$ ) and populations ( $|0_{anti}\rangle$ : blue,  $|0_{syn}\rangle$ : red,  $|2_{lower}\rangle$ : green) for the two-pulse excitation scheme  $|0_{anti}\rangle \rightarrow |2_{lower}\rangle \rightarrow |0_{syn}\rangle$ . The parameters of the two laser pulses are  $\tau_p = 50$  ps,  $t_0 = 100$  ps,  $I_{max} = 150$  MW cm $^{-2}$  and  $\tilde{\nu}_0 = 582.82$  cm $^{-1}$  (first pulse, resonant with the  $|0_{anti}\rangle \leftrightarrow |2_{lower}\rangle$  transition), and  $\tau_p = 80$  ps,  $t_0 = 360$  ps,  $I_{max} = 150$  MW cm $^{-2}$  and  $\tilde{\nu}_0 = 582.00$  cm $^{-1}$  (second pulse, resonant with the  $|0_{syn}\rangle \leftrightarrow |2_{lower}\rangle$  transition). The Gaussian envelope functions (normalized to maximum intensity) of the two sequential laser pulses are shown by the dashed lines.



**Fig. 3** Spectra of the *anti* (blue lines, corresponding to the  $|0_{anti}\rangle$  state) and *syn* (red lines, corresponding to the  $|0_{syn}\rangle$  state) isomers in two different spectral ranges. The relative absorption cross section  $\sigma_{rel}$  is given as a function of the wavenumber  $\tilde{\nu}$ , and the shape of the spectral lines is described by a Gaussian function with a full width at half maximum of  $0.025$  cm $^{-1}$ . At  $t = 0$  only the blue (*anti*) lines appear in the spectrum, whereas at  $t = 500$  ps only the red (*syn*) lines are present in the simulated experiment of Fig. 2, which can thus be easily followed by kinetic infrared spectroscopy.

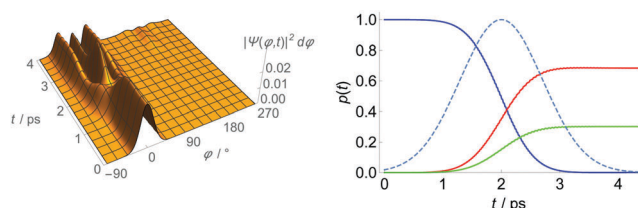


**Fig. 4** Time-dependent wavepacket and populations ( $|0_{anti}\rangle$ : blue,  $|2_{lower}\rangle$ : red,  $|2_{upper}\rangle$ : green) for the excitation scheme  $|0_{anti}\rangle \rightarrow |2_{lower}\rangle$  and  $|2_{upper}\rangle$ . The parameters of the laser pulse are  $\tau_p = 1$  ps,  $t_0 = 2$  ps,  $I_{max} = 250$  GW cm $^{-2}$  and  $\tilde{\nu}_0 = 584.00$  cm $^{-1}$ . The Gaussian envelope function (normalized to maximum intensity) of the laser pulse is shown by the dashed line.

evolution of the wavepacket and selected eigenstate populations. The populations of the  $|0_{anti}\rangle$  and  $|0_{syn}\rangle$  states in the final state are not equal because of the asymmetry in the eigenstates and electric dipole matrix elements.

**3.2.4 Two-pulse excitation scheme:  $|0_{anti}\rangle \rightarrow |2_{lower}\rangle \rightarrow |1_{syn}\rangle$ .** This excitation scheme corresponds to a stimulated resonance Raman-like process and switches between the two localized eigenstates  $|0_{anti}\rangle$  and  $|1_{syn}\rangle$ . The frequencies are chosen to be

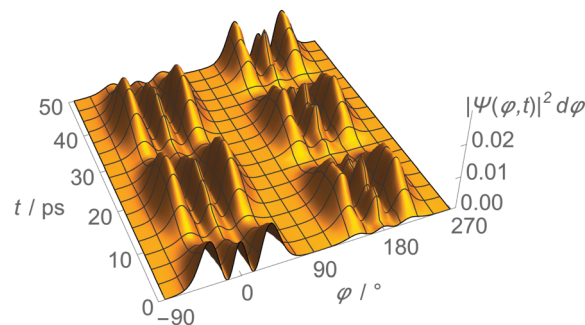


**Fig. 5** Field-free time evolution of the wavepacket generated by the excitation scheme  $|0_{anti}\rangle \rightarrow |2_{lower}\rangle$  and  $|2_{upper}\rangle$ . One recognizes the isomerization due to tunneling within  $10.3$  ps following the simple tunneling time formula  $t_{iso} = h/(2\Delta E)$ .

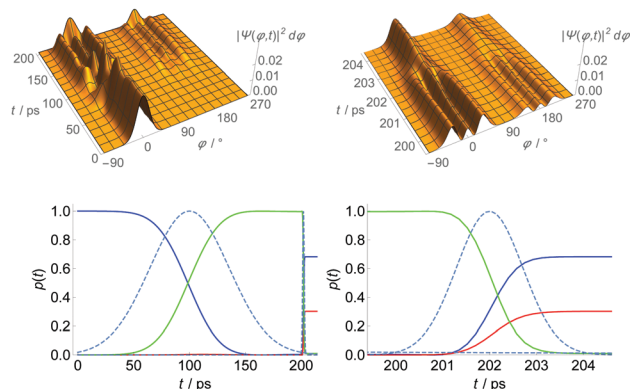


**Fig. 6** Time-dependent wavepacket and populations ( $|0_{anti}\rangle$ : blue,  $|0_{syn}\rangle$ : red,  $|2_{lower}\rangle$ : green) for the two-pulse excitation scheme  $|0_{anti}\rangle \rightarrow |2_{lower}\rangle \rightarrow |0_{anti}\rangle$  and  $|0_{syn}\rangle$ . The parameters of the two laser pulses are  $\tau_p = 50$  ps,  $t_0 = 100$  ps,  $I_{max} = 150$  MW cm $^{-2}$  and  $\tilde{\nu}_0 = 582.82$  cm $^{-1}$  (first pulse, resonant with the  $|0_{anti}\rangle \leftrightarrow |2_{lower}\rangle$  transition), and  $\tau_p = 1$  ps,  $t_0 = 202$  ps,  $I_{max} = 250$  GW cm $^{-2}$  and  $\tilde{\nu}_0 = 582.41$  cm $^{-1}$  (second pulse). The Gaussian envelope functions (normalized to maximum intensity) of the two sequential laser pulses are shown by the dashed lines. Panels on the right show the time evolution of the wavepacket and populations starting from the onset of the second laser pulse.

in exact resonance for the absorption and stimulated emission pulses. Fig. 7 shows the time evolution of the wavepacket and selected eigenstate populations. The second laser pulse is polarized along the  $x(c)$  axis.

### 3.3 Wavepacket dynamics (with the state $|1_{anti}\rangle$ as the initial state)

We use linear polarization along the  $x(c)$  axis throughout Section 3.3 with the state  $|1_{anti}\rangle$  as the initial state unless stated otherwise.

**3.3.1 Two-pulse excitation scheme:  $|1_{anti}\rangle \rightarrow |2_{lower}\rangle \rightarrow |1_{syn}\rangle$ .** Fig. 8 shows the time evolution of the wavepacket and selected eigenstate populations. Here also one finds essentially complete isomerization with transfer to the final *syn* state  $|1_{syn}\rangle$  from the initial *anti* state  $|1_{anti}\rangle$ . The *anti* and *syn* “states” of the switch can be distinguished by measuring the infrared spectrum of the molecule. Simulated spectra for the two

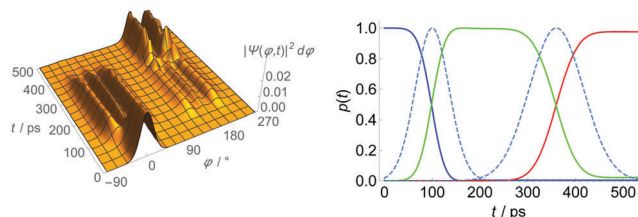


**Fig. 7** Time-dependent wavepacket and populations ( $|0_{anti}\rangle$ : blue,  $|1_{syn}\rangle$ : red,  $|2_{lower}\rangle$ : green) for the two-pulse excitation scheme  $|0_{anti}\rangle \rightarrow |2_{lower}\rangle \rightarrow |1_{syn}\rangle$ . The parameters of the two laser pulses are  $\tau_p = 50$  ps,  $t_0 = 100$  ps,  $I_{max} = 150$  MW cm $^{-2}$  and  $\tilde{\nu}_0 = 582.82$  cm $^{-1}$  (first pulse, resonant with the  $|0_{anti}\rangle \leftrightarrow |2_{lower}\rangle$  transition), and  $\tau_p = 80$  ps,  $t_0 = 360$  ps,  $I_{max} = 1$  MW cm $^{-2}$  and  $\tilde{\nu}_0 = 273.05$  cm $^{-1}$  (second pulse, resonant with the  $|1_{syn}\rangle \leftrightarrow |2_{lower}\rangle$  transition). The Gaussian envelope functions (normalized to maximum intensity) of the two sequential laser pulses are shown by the dashed lines.

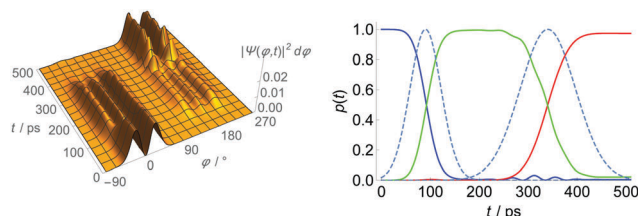


**Fig. 8** Time-dependent wavepacket and populations ( $|1_{anti}\rangle$ : blue,  $|1_{syn}\rangle$ : red,  $|2_{lower}\rangle$ : green) for the two-pulse excitation scheme  $|1_{anti}\rangle \rightarrow |2_{lower}\rangle \rightarrow |1_{syn}\rangle$ . The parameters of the two laser pulses are  $\tau_p = 45$  ps,  $t_0 = 90$  ps,  $I_{max} = 1$  MW cm $^{-2}$  and  $\tilde{\nu}_0 = 273.78$  cm $^{-1}$  (first pulse, resonant with the  $|1_{anti}\rangle \leftrightarrow |2_{lower}\rangle$  transition), and  $\tau_p = 80$  ps,  $t_0 = 340$  ps,  $I_{max} = 1$  MW cm $^{-2}$  and  $\tilde{\nu}_0 = 273.05$  cm $^{-1}$  (second pulse, resonant with the  $|1_{syn}\rangle \leftrightarrow |2_{lower}\rangle$  transition). The Gaussian envelope functions (normalized to maximum intensity) of the two sequential laser pulses are shown by the dashed lines.

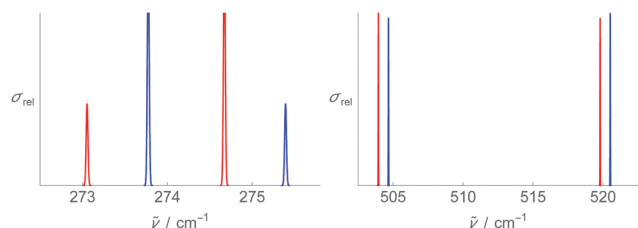


**Fig. 9** Spectra of the *anti* (blue lines, corresponding to the  $|1_{anti}\rangle$  state) and *syn* (red lines, corresponding to the  $|1_{syn}\rangle$  state) isomers in two different spectral ranges. The relative absorption cross section  $\sigma_{rel}$  is given as a function of the wavenumber  $\tilde{\nu}$ , the shape of the spectral lines is described by a Gaussian function with a full width at half maximum of 0.025 cm $^{-1}$ .

isomers (states  $|1_{anti}\rangle$  and  $|1_{syn}\rangle$ ) in two different spectral ranges are shown in Fig. 9. At  $t = 0$  only the *anti* (blue) lines are visible in the spectrum and at  $t = 500$  ps one sees only the *syn* (red) lines.

**3.3.2 Excitation scheme:  $|1_{anti}\rangle \rightarrow |2_{lower}\rangle$  and  $|2_{upper}\rangle$ .** This excitation scheme (Fig. 10 and 11) corresponds to the generation of a localized coherent superposition in the excited tunneling states with  $\nu_T = 2$  ( $|2_{lower}\rangle$  and  $|2_{upper}\rangle$ ) followed by field-free tunneling isomerization. Fig. 10 shows the time evolution of the wavepacket and selected eigenstate populations during the initial excitation process. Fig. 11 depicts the field-free

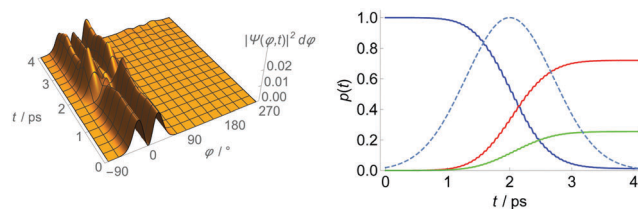


**Fig. 10** Time-dependent wavepacket and populations ( $|1_{anti}\rangle$ : blue,  $|2_{lower}\rangle$ : red,  $|2_{upper}\rangle$ : green) for the excitation scheme  $|1_{anti}\rangle \rightarrow |2_{lower}\rangle$  and  $|2_{upper}\rangle$ . The parameters of the laser pulse are  $\tau_p = 1$  ps,  $t_0 = 2$  ps,  $I_{max} = 1.5$  GW cm $^{-2}$  and  $\tilde{\nu}_0 = 275.00$  cm $^{-1}$ . The Gaussian envelope function (normalized to maximum intensity) of the laser pulse is shown by the dashed line.

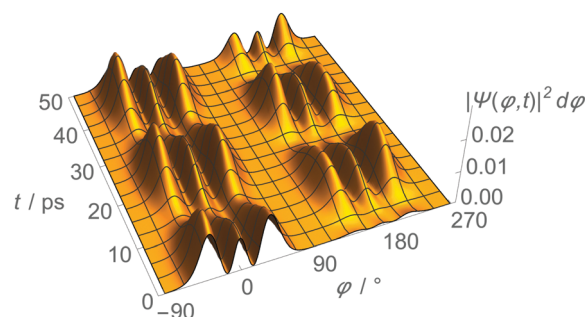


**Fig. 11** Field-free time evolution of the wavepacket generated by the excitation scheme  $|1_{anti}\rangle \rightarrow |2_{lower}\rangle$  and  $|2_{upper}\rangle$ . One recognizes the isomerization due to tunneling within 10.3 ps following the simple tunneling time formula  $t_{iso} = h/(2\Delta E)$ .

time evolution of the coherent superposition of  $|2_{lower}\rangle$  and  $|2_{upper}\rangle$  generated by the laser pulse, corresponding to the isomerization process at longer times.

**3.3.3 Two-pulse excitation scheme:  $|1_{anti}\rangle \rightarrow |2_{lower}\rangle \rightarrow |1_{anti}\rangle$  and  $|1_{syn}\rangle$ .** This excitation scheme corresponds to the preparation of a bistructural superposition state in levels with  $\nu_T = 1$  ( $|1_{anti}\rangle$  and  $|1_{syn}\rangle$ ) at the end of the process. Fig. 12 shows the time evolution of the wavepacket and selected eigenstate populations. During the final part near 184 ps one recognizes the bistructural (time-independent) state.

### 3.4 Preparation of a state with $p_{|0_{anti}\rangle} \approx 0.5$ and $p_{|0_{syn}\rangle} \approx 0.5$ and the time evolution of the spectrum

*meta*-D-Phenol has point group symmetry  $C_s$  with parity as a good quantum number within the electromagnetic theory neglecting electroweak parity violation.<sup>31</sup> However, the purely electronic Born–Oppenheimer potential has  $C_{2v}$  point group symmetry as relevant for the symmetric molecule phenol, where the rovibronic wavefunctions can also be classified in the molecular symmetry group  $M_{s4}$ , isomorphous to  $C_{2v}$ .<sup>31,33</sup> In contrast, the effective channel potential for *m*-D-phenol is slightly asymmetric with the minima differing by  $\Delta E_p/(hc) = 0.90$  cm $^{-1}$  as seen in Fig. 1. This slight asymmetry results in quite asymmetric ground state and low-energy wavefunctions. However, at higher excitations the tunneling sublevel wavefunctions increasingly show the underlying effective  $C_{2v}$  symmetry, as the

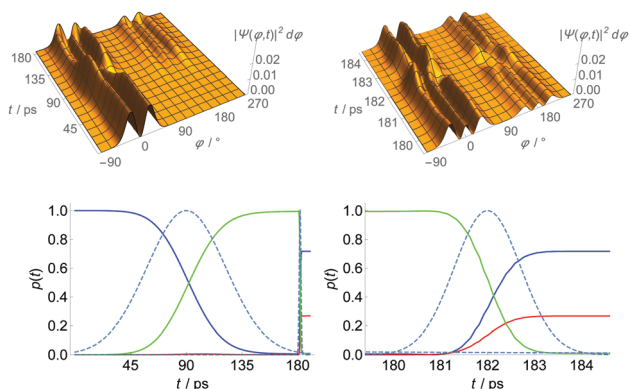


**Fig. 12** Time-dependent wavepacket and populations ( $|1_{anti}\rangle$ : blue,  $|1_{syn}\rangle$ : red,  $|2_{lower}\rangle$ : green) for the two-pulse excitation scheme  $|1_{anti}\rangle \rightarrow |2_{lower}\rangle \rightarrow |1_{anti}\rangle$  and  $|1_{syn}\rangle$ . The parameters of the two laser pulses are  $\tau_p = 45$  ps,  $t_0 = 90$  ps,  $I_{max} = 1$  MW cm $^{-2}$  and  $\tilde{\nu}_0 = 273.78$  cm $^{-1}$  (first pulse, resonant with the  $|1_{anti}\rangle \leftrightarrow |2_{lower}\rangle$  transition), and  $\tau_p = 1$  ps,  $t_0 = 182$  ps,  $I_{max} = 1.75$  GW cm $^{-2}$  and  $\tilde{\nu}_0 = 273.41$  cm $^{-1}$  (second pulse). The Gaussian envelope functions (normalized to maximum intensity) of the two sequential laser pulses are shown by the dashed lines. Panels on the right show the time evolution of the wavepacket and populations starting from the onset of the second laser pulse.

tunneling splitting becomes much larger than the asymmetry in the potential ( $\Delta E_T > \Delta E_P$ ). This can be nicely seen in Fig. 1 for the  $v_T = 3$  levels, where the wavefunction is approximately symmetric with respect to the  $xz$  plane (the point  $\varphi = 90^\circ$  in Fig. 1) for the lower tunneling sublevel and approximately antisymmetric for the upper sublevel. The wavefunctions thus can be labelled  $A$  (symmetric) or  $B$  (antisymmetric) approximately as in phenol, where this symmetry is exact. This results in an approximate selection rule for short-pulse radiative transitions for stimulated emission from a tunneling sublevel  $3_A = 3_l$  or  $3_B = 3_u$  to the ground state, preparing an approximately symmetric or antisymmetric superposition state of the ground-state wavefunctions.

Fig. 13 shows the time evolution of the wavepacket and selected eigenstate populations for the excitation scheme  $|0_{anti}\rangle \rightarrow |3_{lower}\rangle \rightarrow |0_{anti}\rangle$  and  $|0_{syn}\rangle$ . We use  $|3_{lower}\rangle$  as the intermediate state to obtain almost equal populations  $p_{|0_{anti}\rangle}$  and  $p_{|0_{syn}\rangle}$  in the final state generated by the two laser pulses.

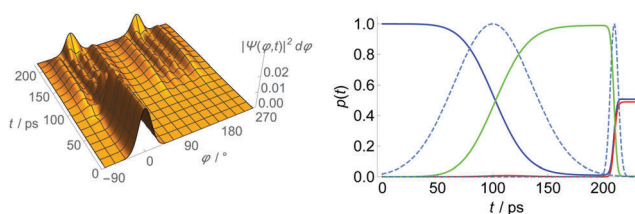


**Fig. 13** Time-dependent wavepacket and populations ( $|0_{anti}\rangle$ : blue,  $|0_{syn}\rangle$ : red,  $|3_{lower}\rangle$ : green) for the two-pulse excitation scheme  $|0_{anti}\rangle \rightarrow |3_{lower}\rangle \rightarrow |0_{anti}\rangle$  and  $|0_{syn}\rangle$ . The parameters of the two laser pulses are  $\tau_p = 50$  ps,  $t_0 = 100$  ps,  $I_{max} = 1$  GW cm $^{-2}$  and  $\tilde{\nu}_0 = 813.72$  cm $^{-1}$  (first pulse, resonant with the  $|0_{anti}\rangle \leftrightarrow |3_{lower}\rangle$  transition), and  $\tau_p = 5$  ps,  $t_0 = 210$  ps,  $I_{max} = 60$  GW cm $^{-2}$  and  $\tilde{\nu}_0 = 813.10$  cm $^{-1}$  (second pulse). The Gaussian envelope functions (normalized to maximum intensity) of the two sequential laser pulses are shown by the dashed lines.

While the probability densities and populations after the end of the second pulse do not change any more, the effective symmetry of the wavefunction does (changing between  $A$  and  $B$ ) as does the spectrum because of the dipole selection rules and transition moments.

Fig. 14 and 15 show the corresponding time dependence of the spectrum in the 581–585 cm $^{-1}$  and 810–835 cm $^{-1}$  ranges for one period ( $T = h/(E_{0,syn} - E_{0,anti}) = 40.46$  ps is the oscillation period of the beating between  $|0_{anti}\rangle$  and  $|0_{syn}\rangle$ ). Spectral lines in this range correspond to transitions between the eigenstates  $|0_{anti}\rangle$  and  $|0_{syn}\rangle$ , and  $|3_{lower}\rangle$  and  $|3_{upper}\rangle$  (810–830 cm $^{-1}$ ) and  $|2_{lower}\rangle$  and  $|2_{upper}\rangle$  (580–585 cm $^{-1}$ ). The initial state was prepared by the process shown in Fig. 13. The relative phase between  $|0_{syn}\rangle$

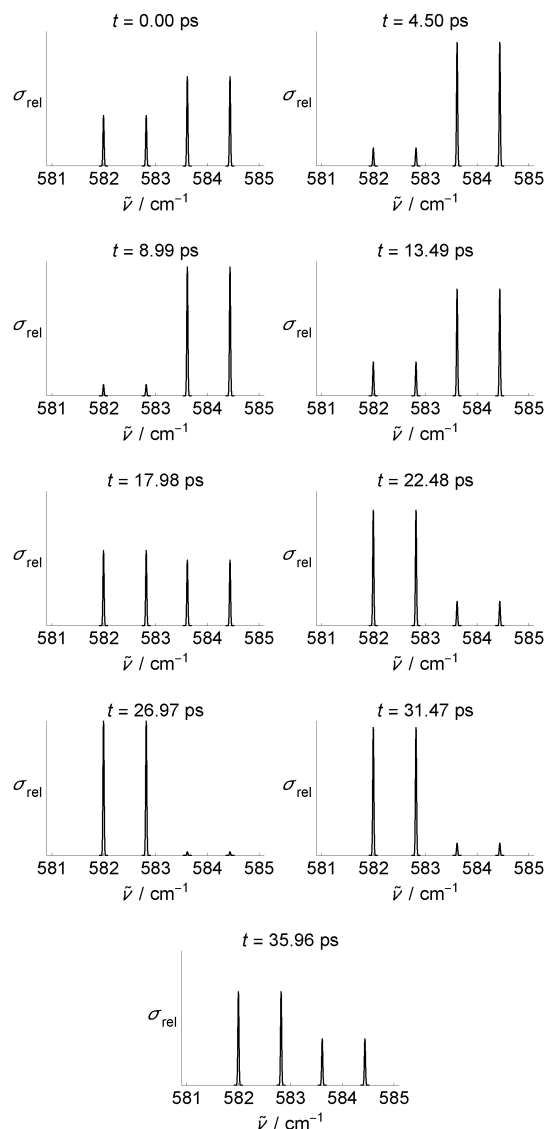


**Fig. 14** Spectra as a function of time for one oscillation period (see text). The initial time  $t = 0$  ps of the field-free dynamics corresponds to the end of the second laser pulse of the scheme  $|0_{anti}\rangle \rightarrow |3_{lower}\rangle \rightarrow |0_{anti}\rangle$  and  $|0_{syn}\rangle$  at  $t = 220$  ps. The relative absorption cross section  $\sigma_{rel}$  is given as a function of the wavenumber  $\tilde{\nu}$ , and the shape of the spectral lines is described by a Gaussian function with a full width at half maximum of 0.025 cm $^{-1}$ .

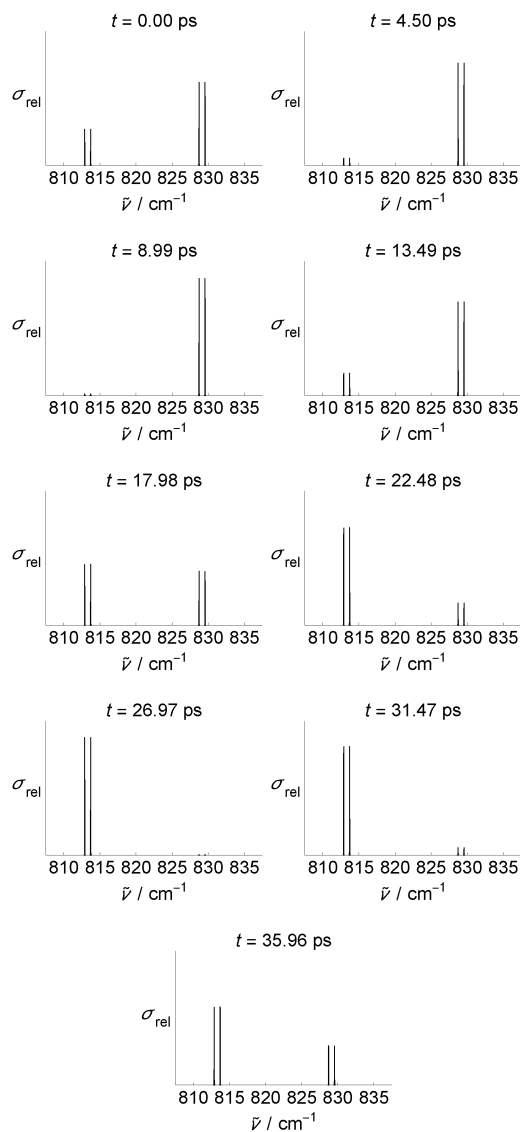


Fig. 15 Spectra as a function of time for one oscillation period (see text). The initial time  $t = 0$  ps of the field-free dynamics corresponds to the end of the second laser pulse of the scheme  $|0_{anti}\rangle \rightarrow |3_{lower}\rangle \rightarrow |0_{anti}\rangle$  and  $|0_{syn}\rangle$  at  $t = 220$  ps. The relative absorption cross section  $\sigma_{rel}$  is given as a function of the wavenumber  $\tilde{\nu}$ , and the shape of the spectral lines is described by a Gaussian function with a full width at half maximum of  $0.025$   $\text{cm}^{-1}$ .

and  $|0_{anti}\rangle$  after the end of the second pulse ( $t = 220$  ps), which defines the time zero for the following field-free time evolution, is  $68.7^\circ$ . Although the populations of the levels and the concentrations of the *syn* and *anti* isomers do not change after 220 ps (equivalent to 0 ps in Fig. 14 and 15), there is a pronounced change in the absorption spectrum because of the change in the approximate symmetry of the wavefunction (“A” or “B”).

## 4 Conclusions

We have shown here that with coherent radiative excitation of *meta*-D-phenol in the infrared spectral range one can realize a quasiclassical molecular switch, which works on the basis of

the simple *anti*  $\rightarrow$  *syn* isomerization process, which can be probed by straightforward absorption spectroscopy, because of the slight difference in the absorption spectra of these isomers. The spectroscopic probing can also be considered to be a “readout process” in the corresponding storage based on the switch between molecular structures. Given the spectral changes arising also with the excitation of other vibrational modes (for instance, CO stretching or OH stretching) based on the quadiabatic channel RPH predictions, such a readout could also be carried out in quite different spectral ranges. These observations can all be easily understood qualitatively with a simple picture of the expected changes in the infrared spectrum upon isomerization. They are consistent with our usual qualitative picture of molecular switches as quasiclassical molecular structures,<sup>1</sup> even though we have here an important influence of quantum effects due to tunneling in this molecule.

The second demonstration of the quantum switch is based on a more profound quantum effect, the generation of a non-classical superposition state of the two isomeric structures in their ground state, which evolves in time due to their energy difference and can be probed by ordinary linear absorption spectroscopy in the time domain. The changes in the absorption spectrum are related to a time-dependent change in the symmetry of the wavefunction which is furthermore related to the approximate symmetry of the underlying molecular Hamiltonian. The situation is, in principle, similar to the time-dependent change of parity in chiral molecules, where, however, the asymmetry is by more than 10 orders of magnitude smaller, as the parity symmetry of the underlying Hamiltonian is almost perfect (but not exactly so).<sup>25,26,31</sup> In this sense, the present results can also be used as a simple testing ground for the future experiments on molecular parity violation. Interestingly, the two transition structures (at  $+90^\circ$  and at  $-90^\circ$ , Fig. 1) are isotopically chiral with two enantiomeric forms of different energies, in principle, although the parity violating difference in the effective potential is expected to be minute, on the order of less than  $(hc)10^{-12}$   $\text{cm}^{-1}$  (see ref. 31, 43 and 44). A further obvious test could concern the rate of the collisional dephasing in the time-dependent wavefunction after 220 ps at the end of the preparation process in Fig. 13. This dephasing is expected to be fast and would result in an equilibration of the time-dependent spectrum shown in Fig. 14 and 15 reaching a stationary state at the end. Such an experiment could be carried out in a molecular beam setup as presented in ref. 26, allowing for some addition of a background gas in the expansion chamber. In this sense, the quantum switch based on superposition states would be sensitive to external perturbations, and thus could be used in a transient application, whereas the quasiclassical quantum switch based on isomers is rather stable and might also be used for a more permanent storage.

## Conflicts of interest

There are no conflicts to declare.

## Acknowledgements

Our work was supported financially by the Swiss National Science Foundation, ETH Zürich, an ERC Advanced Grant (No. 290925), the COST project MOLIM and NKFIH (Grant No. PD124699). C. F. is grateful to COST Project No. CM1405, MOLIM: Molecules in Motion for funding a short-term scientific mission at ETH Zürich. We thank Irina Bolotova, Attila G. Császár, Carine Manca Tanner, Roberto Marquardt, Frédéric Merkt and Georg Seyfang for help and discussion.

## References

- 1 *Molecular Switches*, ed. B. L. Feringa and W. R. Browne, Wiley-VCH Verlag GmbH & Co. KGaA, 2nd edn, 2011.
- 2 Y. Hirshberg, *C. R. Acad. Sci.*, 1950, **231**, 903–904.
- 3 J. Ronayette, R. Arnaud, P. Lebourgeois and J. Lemaire, *Can. J. Chem.*, 1974, **52**, 1848–1857.
- 4 F. Hamon, F. Djedaini-Pilard, F. Barbot and C. Len, *Tetrahedron*, 2009, **65**, 10105–10123.
- 5 F. Hamon, F. Djedaini-Pilard, F. Barbot and C. Len, *Tetrahedron*, 2010, **66**, 2538.
- 6 S. Shinkai and O. Manabe, in *Photocontrol of ion extraction and ion transport by photofunctional crown ethers*, ed. F. Vögtle and E. Weber, Springer Berlin Heidelberg, Berlin, Heidelberg, 1984, pp. 67–104.
- 7 S. Shinkai, T. Nakaji, T. Ogawa, K. Shigematsu and O. Manabe, *J. Am. Chem. Soc.*, 1981, **103**, 111–115.
- 8 S. Shinkai, T. Ogawa, Y. Kusano, O. Manabe, K. Kikukawa, T. Goto and T. Matsuda, *J. Am. Chem. Soc.*, 1982, **104**, 1960–1967.
- 9 E. H. G. Backus, R. Bloem, P. M. Donaldson, J. A. Ihalainen, R. Pfister, B. Paoli, A. Caffisch and P. Hamm, *J. Phys. Chem. B*, 2010, **114**, 3735–3740.
- 10 W. Song, C. J. Querebillo, R. Götz, S. Katz, U. Kuhlmann, U. Gernert, I. M. Weidinger and P. Hildebrandt, *Nanoscale*, 2017, **9**, 8380–8387.
- 11 D. Oesterheld, P. Hegemann, P. Tavan and K. Schulten, *Eur. Biophys. J.*, 1986, **14**, 123–129.
- 12 M. Quack, *Time and Time Reversal Symmetry in Quantum Chemical Kinetics*, in *Fundamental World of Quantum Chemistry*, Kluwer Academic Publishers, Dordrecht, 2004, vol. 3, pp. 423–474.
- 13 W. R. Browne and B. L. Feringa, *Chiroptical Molecular Switches*, in *Molecular Switches*, Wiley-VCH Verlag GmbH & Co. KGaA, 2011, pp. 121–179.
- 14 V. A. Azov and F. Diederich, *Switching Processes in Cavitands, Containers and Capsules*, in *Molecular Switches*, Wiley-VCH Verlag GmbH & Co. KGaA, 2011, pp. 257–300.
- 15 W. Szymański, J. M. Beierle, H. A. V. Kistemaker, W. A. Velema and B. L. Feringa, *Chem. Rev.*, 2013, **113**, 6114–6178.
- 16 B. L. Feringa, *J. Org. Chem.*, 2007, **72**, 6635–6652.
- 17 D. B. Amabilino, C. O. Dietrich-Buchecker, A. Livoreil, L. Pérez-García, J.-P. Sauvage and J. F. Stoddart, *J. Am. Chem. Soc.*, 1996, **118**, 3905–3913.
- 18 B. L. Feringa, *Angew. Chem., Int. Ed.*, 2017, **56**, 11060–11078.
- 19 J.-P. Sauvage, *Angew. Chem., Int. Ed.*, 2017, **56**, 11080–11093.
- 20 J. F. Stoddart, *Angew. Chem., Int. Ed.*, 2017, **56**, 11094–11125.
- 21 T. Kudernac, N. Ruangsapapichat, M. Parschau, B. Maciá, N. Katsonis, S. R. Harutyunyan, K.-H. Ernst and B. L. Feringa, *Nature*, 2011, **479**, 208–211.
- 22 R. R. Ernst, G. Bodenhausen and A. Wokaun, *Principles of Nuclear Magnetic Resonance in One and Two Dimensions*, University Press, Oxford, 1987.
- 23 A. Schweiger and G. Jeschke, *Principles of Pulse Electron Paramagnetic Resonance*, University Press, Oxford, 2001.
- 24 M. Quack, *Adv. Chem. Phys.*, 1982, **50**, 395–473.
- 25 R. Prentner, M. Quack, J. Stohner and M. Willeke, *J. Phys. Chem. A*, 2015, **119**, 12805–12822.
- 26 P. Dietiker, E. Miloglyadov, M. Quack, A. Schneider and G. Seyfang, *J. Chem. Phys.*, 2015, **143**, 244305.
- 27 N. V. Vitanov, A. A. Rangelov, B. W. Shore and K. Bergmann, *Rev. Mod. Phys.*, 2017, **89**, 015006.
- 28 K. Bergmann, H. Theuer and B. W. Shore, *Rev. Mod. Phys.*, 1998, **70**, 1003–1025.
- 29 W. Dong, N. Mukherjee and R. N. Zare, *J. Chem. Phys.*, 2013, **139**, 074204.
- 30 R. Marquardt and M. Quack, *Z. Phys. D*, 1996, **36**, 229–237.
- 31 M. Quack, *Fundamental Symmetries and Symmetry Violations from High Resolution Spectroscopy*, in *Handbook of High-resolution Spectroscopy*, John Wiley & Sons, Ltd, 2011, vol. 1, pp. 659–722.
- 32 M. Quack, *Molecular femtosecond quantum dynamics between less than yoctoseconds and more than days: Experiment and theory*, in *Femtosecond Chemistry*, Verlag Chemie, Weinheim, 1994, pp. 781–818.
- 33 S. Albert, P. Lerch, R. Prentner and M. Quack, *Angew. Chem., Int. Ed.*, 2013, **52**, 346–349.
- 34 S. Albert, Z. Chen, C. Fábri, P. Lerch, R. Prentner and M. Quack, *Mol. Phys.*, 2016, **114**, 2751–2768.
- 35 M. Nielsen and I. Chuang, *Quantum Computation and Quantum Information*, Cambridge University Press, 2000.
- 36 S. Albert, K. K. Albert, H. Hollenstein, C. M. Tanner and M. Quack, *Fundamentals of Rotation-Vibration Spectra*, in *Handbook of High-resolution Spectroscopy*, John Wiley & Sons, Ltd, 2011, vol. 1, pp. 117–173.
- 37 B. Fehrensens, D. Luckhaus and M. Quack, *Chem. Phys. Lett.*, 1999, **300**, 312–320.
- 38 B. Fehrensens, D. Luckhaus and M. Quack, *Z. Physik. Chem.*, 1999, **209**, 1–19.
- 39 B. Fehrensens, D. Luckhaus and M. Quack, *Chem. Phys.*, 2007, **338**, 90–105.
- 40 R. Meyer, *J. Chem. Phys.*, 1970, **52**, 2053–2059.
- 41 Wolfram Research, Inc., Mathematica 10.4, <https://www.wolfram.com>.
- 42 F. Merkt and M. Quack, *Molecular Quantum Mechanics and Molecular Spectra, Molecular Symmetry, and Interaction of Matter with Radiation*, in *Handbook of High-resolution Spectroscopy*, John Wiley & Sons, Ltd, 2011, vol. 1, pp. 1–55.
- 43 R. Berger, M. Quack, A. Sieben and M. Willeke, *Helv. Chim. Acta*, 2003, **86**, 4048–4060.
- 44 R. Berger, G. Laubender, M. Quack, A. Sieben, J. Stohner and M. Willeke, *Angew. Chem., Int. Ed.*, 2005, **44**, 3623–3626.